International Journal of Heat and Mass Transfer 181 (2021) 121850

Contents lists available at ScienceDirect

International Journal of Heat and Mass Transfer

journal homepage: www.elsevier.com/locate/hmt

Leveraging the entropy generation minimization and designed porous media for the optimization of heat sinks employed in low-grade waste heat harvesting

Kleber Marques Lisboa [a,*], José Luiz Zanon Zotin [b], Carolina P. Naveira-Cotta [c], Renato Machado Cotta [c,d]

[a] Laboratory of Thermal Sciences (LATERMO), Department of Mechanical Engineering (TEM/PGMEC), Universidade Federal Fluminense, UFF, Niterói, RJ, Brazil
[b] Centro Federal de Educação Tecnológica Celso Suckow da Fonseca, CEFET/RJ, RJ, Brazil
[c] Laboratory of Nano & Microfluidics and Microsystems, LabMEMS, Mechanical Engineering Dept., POLI & COPPE, UFRJ, Federal University of Rio de Janeiro, Brazil
[d] General Directorate of Nuclear and Technological Development, DGDNTM, Brazilian Navy, Ministry of Defense, RJ, Brazil

ARTICLE INFO

Article history:
Received 6 May 2021
Revised 12 July 2021
Accepted 11 August 2021
Available online 23 August 2021

KEYWORDS:
Low-grade waste heat
heat sinks
designed porous media
entropy generation minimization
integral transforms

ABSTRACT

A comprehensive optimization procedure for the design of heat sinks used to harvest low-grade waste heat for secondary processes is proposed. A designed porous medium approach is used, providing modelling versatility and allowing for the treatment of several internal geometries within the same framework. Two applications, taken from the cooling of high concentration photovoltaic cells and membrane distillation, are used to illustrate the proposed procedure. Three internal heat sink geometries, namely plate fins, pin fins, and metal foams, are analyzed, and the selection as to which one is the more advantageous is shown to be dependent on size and operational conditions. Possible pitfalls of a traditional design procedure are pointed out, for heat transfer capability, under high heat load condition, should be emphasized over fluid friction avoidance. The entropy generation rate is then shown to be a reliable metric when designing for low-grade waste heat recovery, automatically focusing on either viscous dissipation or thermal resistance minimization without introducing any artificial figure of merit for that purpose.

© 2021 Elsevier Ltd. All rights reserved.

1. Introduction

Recovery of high-grade waste heat is routinely done in the industry, allowing for a large amount of economic value to be further extracted from the same amount of burnt fuel. On the other hand, low-grade waste heat is often discarded [1], for it would require expensive equipment to effectively cope with the small temperature differences involved, while generating a relatively small amount of useful work, insufficient to justify the investment. However, the challenges posed by climate change altered this scenario and several technologies have been proposed in the last two decades to reuse low-grade waste heat, often in conjunction with renewable energy sources, in secondary processes [2,3]. Amongst these processes one may cite organic Rankine cycles [4], water desalination using membrane distillation [5], thermoelectric generation [6], etc.

Given a certain choice of processes, harnessing low-grade waste heat and the associated low exergy content may benefit that the equipment employed in its recovery destroy the least possible amount of the already depleted available work. Therefore, for this kind of application, the use of the Entropy Generation Minimization (EGM) method [7] in the design of each component involved is beneficial. EGM is based on introducing the inexorable irreversibility of fluid flow and heat transfer processes into relations from Thermodynamics to find the best possible design given a set of constraints, like size [7].

One component commonly used in low-grade waste heat harvesting is the heat sink. For instance, in high concentration photovoltaic (HCPV) cells, the potential for reuse of the waste heat delivered to the coolant via a heat sink attached to the back of each cell was demonstrated to be significant [3]; a similar application can be found in electronic cooling [2]. Due to the large heat loads involved in both these applications, most of the related research focused on minimizing the thermal resistance of the heat sinks [8-10]. Nonetheless, minimization of entropy generation has also been addressed for plate-fins- [11,12], pin-fins- [13,14], and

* Corresponding author
E-mail address: kmlisboa@id.uff.br (K.M. Lisboa).

https://doi.org/10.1016/j.ijheatmasstransfer.2021.121850
0017-9310/© 2021 Elsevier Ltd. All rights reserved.

Nomenclature

a_{fs}	Specific surface area
b	Width of the channel
c_F	Inertial coefficient
c_p	Specific heat at constant pressure of the fluid
d	Height of the porous medium channel
d_c	Pin diameter
d_{fib}	Fiber diameter
d_p	Pore diameter
D_h	Hydraulic diameter
h_{fs}	Interstitial heat transfer coefficient
k	Thermal conductivity
k_d	Apparent thermal conductivity due to thermal dispersion
$k_{fe,x}$	Effective thermal conductivity of the fluid phase in the x-direction
$k_{fe,y}$	Effective thermal conductivity of the fluid phase in the y-direction
$k_{se,x}$	Effective thermal conductivity of the solid phase in the x-direction
$k_{se,y}$	Effective thermal conductivity of the solid phase in the y-direction
K	Permeability of the porous medium
L	Length of the heat sink
$\mathcal{L}$	Lagrangian
M	Number of constraints
N	Truncation order of eigenfunction expansion
Nu	Local Nusselt number
Nu_{fs}	Interstitial Nusselt number
p	Intrinsic average pressure
Pr	Prandtl number
q_w	Heat flux at the bottom wall
Q	Volumetric flow rate
Re_{d_c}	Reynolds number based on the fin diameter
R_{th}	Thermal resistance
$\dot{S}''_{ger,av}$	Average entropy generation rate per unit of planform area
$\dot{S}'''_{ger}$	Local entropy generation rate
$\dot{S}'''_{ger,T}$	Local entropy generation rate associated with heat transfer
$\dot{S}'''_{ger,u}$	Local entropy generation rate associated with fluid flow
T	Temperature field
T_c	Characteristic temperature
T_{in}	Temperature at the inlet
T_m	Mean fluid temperature
u	Seepage velocity vector in the porous medium
$u_{\max}$	Maximum interstitial velocity
w	Width of the porous medium filled channel
$\dot{W}_p$	Pumping power
x	Longitudinal spatial coordinate
y	Transversal spatial coordinate

Greek Symbols

α	Aspect ratio of the channel
ε	Porosity of the porous medium
θ	Temperature under thermally developed flow conditions
μ	Dynamic viscosity of the fluid
ρ	Fluid density
Φ	Viscous dissipation
$\boldsymbol{\chi}$	Vector of design parameters
ψ	Eigenfunctions for the temperature field

Superscripts and subscripts

$-$	Transformed quantity
$\sim$	Normalized quantity
i,j	Indices for the eigenfunction ψ
f	Refers to the fluid phase
s	Refers to the solid phase

metal-foams-based heat sinks [15,16]. Yet, no comprehensive design procedure capable of dealing with any internal morphology of the heat sink, including direct comparison of different configurations, was made available in those works. Moreover, an application of the EGM in heat pipes for waste heat recovery from air conditioning units was recently reported [17].

Heat sinks often require several fins or complex structures to be employed, hindering direct simulation due to the associated elevated computational cost. Additionally, the intensification of transport processes associated with small length scales frequently leads to optimized internal features that are much smaller than the characteristic size of the heat sink itself. These facts open the opportunity to treat the heat sink as a designed porous medium [18]. In this context, a common procedure has been to treat these devices as a channel filled with fluid saturated porous medium and introduce information about the internal structure through effective porous media properties, such as permeability, inertial coefficient, and effective thermal conductivity [9,10,19]. The advantages of adopting the designed porous medium concept of heat sinks make it ideal for computationally intensive tasks and allows for the treatment of different internal morphologies of heat sinks with the same modeling structure.

In theoretical analyses of heat transfer in porous media, the local thermal equilibrium (LTE) hypothesis is usually adopted [20,21]. This formulation neglects the difference between the local solid and fluid temperatures, allowing for the merging of all heat transfer information into a single partial differential transport equation. However, several applications may induce significant deviations from the LTE hypothesis, most notably for large thermal conductivity differences [21-23], which is typically the case for heat sinks. For these cases, local thermal non-equilibrium (LTNE) formulations, consisting of a two-equation heat transfer model, must be employed, adding difficulty to the analysis.

The thermodynamic optimization using EGM can become more informative, in some cases even yielding explicit relations for the optimized parameters and objective function, if analytical solutions are available for the proposed model of the physical situation under analysis [7]. However, analytical solutions to fluid flow and heat transfer problems are usually restricted to simple linear problems in regular geometries; for more involved problems, numerical methods are usually required. Aiming at bridging the gap between analytical and numerical approaches, the Generalized Integral Transform Technique (GITT) was developed [24]. The GITT enabled the extension of the Classical Integral Transform Technique (CITT) to nonlinear problems, irregular geometries, the boundary layer and the Navier-Stokes equations, among others [25]. Furthermore, this hybrid numerical-analytical approach was extended to handle different classes of flow and transport problems involving domains totally filled with fluid saturated porous media [26] and, afterwards, also partially filled porous media [27]. In such developments, the local thermal equilibrium (LTE) hypothesis was employed in writing the governing equations, but LTNE formulations were more recently considered and solved by GITT [28]. The latter proposed a method to deal with LTNE formulations using a single eigenvalue problem, which proved quite effective, enabling the solution of the two-equation model for roughly the same computational cost when the LTE hypothesis is adopted [28].

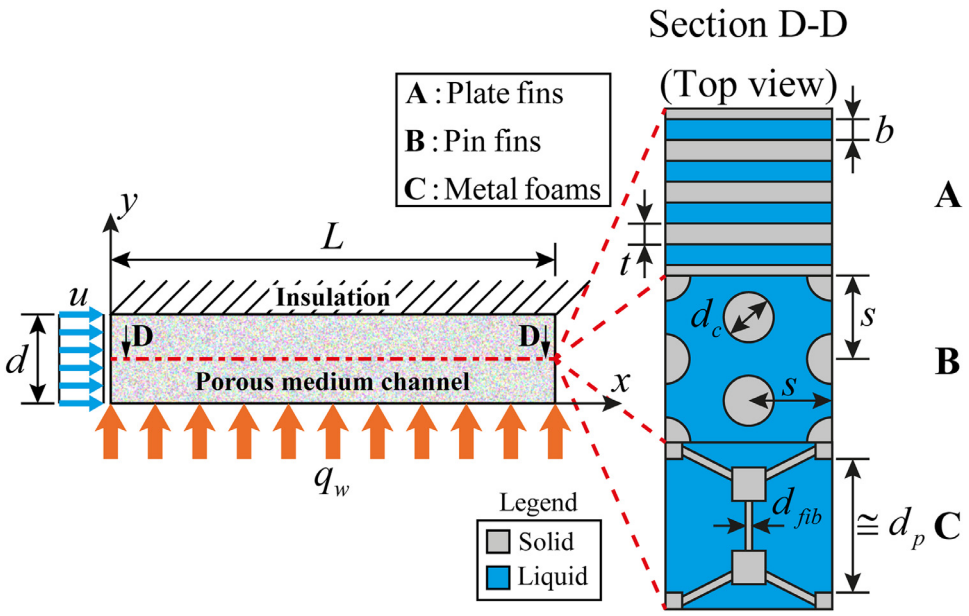

Fig. 1. Porous medium model for three different internal morphologies. A Cartesian coordinate system, main dimensions, the inlet velocity distribution, constant heat flux at the bottom, and insulation at the top are indicated. Top views of the different morphologies: (A) Plate fins; (B) Pin fins; (C) Metal foams.

In this work, a thermodynamic optimization procedure is proposed to obtain ideal internal arrangements for heat sinks responsible for harvesting low-grade waste heat and delivering it to a secondary process. Two different fin configurations, namely plate fins and pin fins, and metal foams are analyzed and critically compared using the entropy generation rate as the main metric. For this purpose, the heat sink is modeled as a fluid saturated porous medium under the LTNE formulation, allowing for the different morphologies to be treated under the same framework. The resulting set of partial differential equations is then solved through the GITT. After validation of the model and computational code developed, a zeroth order approximate solution stemming from the eigenfunction expansion of the GITT is used in the constrained optimization procedure. Finally, assessment of two possible applications of heat sinks in the recovery of low-grade waste heat and comparisons with a traditional sizing procedure are offered.

2. Model and methods

2.1. Porous medium model

Adopting the designed porous medium approach [9,10,18], the solid and liquid phases inside the heat sink are treated as a fluid-saturated porous medium channel, as illustrated in Fig. 1. The properties of the porous medium are dependent on the particular internal morphology of the heat sink. In this work, three different configurations shall be analyzed, namely plate fins, pin fins, and metal foams, as indicated in Fig. 1. The Cartesian coordinate system and main dimensional parameters are also depicted to ease the understanding of the model.

2.1.1. Fluid flow model

The fluid flow model adopted stems from fully saturated porous medium flow theory. More specifically, the Darcy model with Dupuit-Forchheimer form drag term is proposed to model the fluid flow through the porous medium channel of Fig. 1. A macroscopic viscous term, coined as the Brinkman correction, is frequently adopted in analyses of the fluid flow in porous media. However, this term was shown to be usually small and its use is poorly justified for most applications [29,30]. Furthermore, the flow is assumed to be incompressible and fully developed. In sum, we then have,

$$-\frac{dp}{dx} = \frac{\mu}{K}u + \frac{\rho}{K^{1/2}}c_F u^2 \tag{1}$$

where x is the longitudinal coordinate, u is the seepage velocity vector in the porous medium channel, p is the intrinsic pressure, K is the permeability of the porous medium in the x-direction, c_F is the inertial coefficient, ρ is the fluid density, and μ is the dynamic viscosity of the fluid.

As illustrated in Fig. 1, the velocity profile associated with the fully developed flow will be uniform in the y-direction. Therefore, the seepage velocity can be related to the incident flow rate in the following way:

$$u = \frac{Q}{wd} \tag{2}$$

where Q is the volumetric flow rate, and d and w are the height and width of the porous medium channel, respectively. Eqs. (1) and (2) together with the knowledge that the pressure gradient is constant along x, can be employed to determine the pressure drop along the length of the heat sink, as shown below:

$$\Delta p = \frac{\mu}{K}\frac{Q}{wd}L + \frac{\rho}{K^{1/2}}c_F\left(\frac{Q}{wd}\right)^2 L \tag{3}$$

where Δp is the pressure drop between the inlet and the outlet of the heat sink, and L is the length of the heat sink.

The pumping power needed to drive the coolant through the heat sink can then be determined by the multiplication of the pressure drop by the flow rate, as follows:

$$\dot{W}_p = Q\Delta p = \frac{\mu}{K}\frac{Q^2}{wd}L + \frac{\rho}{K^{1/2}}c_F\frac{Q^3}{w^2d^2}L \tag{4}$$

where $\dot{W}_p$ is the pumping power.

2.1.2. Heat transfer model

Heat sinks usually present a large difference between solid and fluid thermal conductivities, which is one of the main criteria for the existence of a significant deviation from the LTE hypothesis [21-23], thereby requiring LTNE formulations. The thermophysical properties are assumed to be constant and the porous medium

is considered to be orthotropic, with its principal axes coinciding with the Cartesian coordinate system axes in Fig. 1. The porous channel is assumed to be wide enough so the heat transfer can be considered to be two-dimensional in the x-y plane of Fig. 1. Viscous dissipation is also taken into account in the form proposed by [31]. The heat transfer model for both the solid and fluid phases then becomes,

$$k_{se,x}\frac{\partial^2 T_s}{\partial x^2}+k_{se,y}\frac{\partial^2 T_s}{\partial y^2}-a_{fs}h_{fs}\left[T_s(x,y)-T_f(x,y)\right]=0 \tag{5.a}$$

$$\rho c_p u\frac{\partial T_f}{\partial x}=k_{fe,x}\frac{\partial^2 T_f}{\partial x^2}+k_{fe,y}\frac{\partial^2 T_f}{\partial y^2}-a_{fs}h_{fs}\left[T_f(x,y)-T_s(x,y)\right]+\Phi \tag{5.b}$$

with,

$$\Phi=\frac{\mu}{K}u^2+\frac{\rho}{K^{1/2}}c_F u^3 \tag{5.c}$$

where y is the transversal coordinate, c_p is the specific heat at constant pressure of the fluid, T_s is the local temperature of the solid phase, T_f is the local temperature of the fluid phase, $k_{se,x}$ is the effective thermal conductivity of the solid phase in the x-direction, $k_{se,y}$ is the effective thermal conductivity of the solid phase in the y-direction, $k_{fe,x}$ is the effective thermal conductivity of the fluid phase in the x-direction, $k_{fe,y}$ is the effective thermal conductivity of the fluid phase in the y-direction, a_{fs} is the specific surface area of the porous channel, h_{fs} is the interstitial heat transfer coefficient, and Φ is the viscous dissipation term. It is noteworthy that the effective thermal conductivities of the fluid may include a thermal dispersion term.

At the entrance of the porous channel of Fig. 1, the fluid is assumed to have a uniform temperature, while the solid is assumed to be locally in thermal equilibrium with the fluid. No outlet condition is prescribed at $x=L$; instead, to avoid the imposition of a possibly unrealistic zero-gradient boundary condition at this point, a limited gradient at $x\to\infty$ is adopted. At the top of the porous channel, an adiabatic boundary condition is imposed. At the bottom wall, as depicted in Fig. 1, a uniform heat flux is prescribed. For LTE formulations, the establishment of this kind of boundary condition is rather simple. However, for LTNE formulations a question arises as to how the heat flux is distributed among the two phases [32]. In this work, the model for this boundary condition assumes local thermal equilibrium between the solid and fluid phases at the boundary and that the heat flux is distributed in accordance with the relative magnitude of the effective thermal conductivity of each phase [33]. The resulting boundary conditions for both the fluid and solid temperatures are as follows:

$$T_f(0,y)=T_s(0,y)=T_{in} \tag{6.a.b}$$

$$\left.\frac{\partial T_f}{\partial x}\right|_{x\to\infty},\left.\frac{\partial T_s}{\partial x}\right|_{x\to\infty}\ \text{limited} \tag{6.c.d}$$

$$T_f(x,0)=T_s(x,0);q_w=-k_{se,y}\left.\frac{\partial T_s}{\partial y}\right|_{y=0}-k_{fe,y}\left.\frac{\partial T_f}{\partial y}\right|_{y=0} \tag{6.e.f}$$

$$\left.\frac{\partial T_f}{\partial y}\right|_{y=d}=\left.\frac{\partial T_s}{\partial y}\right|_{y=d}=0 \tag{6.g.h}$$

where T_{in} is the uniform temperature at the inlet, and q_w is the uniform heat flux imposed at the bottom wall.

The mean fluid temperature, for the present plug flow model, can be determined from the local fluid temperature in the following way:

$$T_m(x)=\frac{1}{d}\int_0^d T_f(x,y)dy \tag{7}$$

where T_m is the mean fluid temperature.

From the definition of the mean fluid temperature, it is possible to establish a relation for the local Nusselt number as,

$$Nu=\frac{q_w}{T_f(x,0)-T_m(x)}\frac{d}{k_{fe,y}} \tag{8}$$

where Nu is the local Nusselt number.

Another important parameter for the evaluation of heat sinks is the thermal resistance, which is defined as follows,

$$R_{th}=\frac{T_f(L,0)-T_{in}}{q_w} \tag{9}$$

where R_{th} is the thermal resistance. The maximum wall temperature is assumed to occur at the bottom right corner of the channel of Fig. 1 in Eq. (9).

2.2. Properties of the equivalent porous medium

The designed porous media concept allowed for the establishment of a common set of governing equations in sections 2.1.1 and 2.1.2. The distinction among the internal morphologies of the heat sink is then accomplished through effective porous medium properties associated with each of the geometries illustrated on the right side of Fig. 1. The resulting properties will be presented in the following subsections.

2.2.1. Plate fins

Due to entrance effects, the prevalence of a thermally developing flow condition in plate fins heat sinks was experimentally established [34]. Therefore, the hydraulic properties for this situation will be determined from results for fully developed flow in rectangular channels. Using the Poiseuille number expression appropriate for laminar flow in rectangular channels [35] and Darcy's law, we can write,

$$K=\frac{\varepsilon b^2}{12}\left[1-\frac{192}{\pi^5}\sum_{i=1,3,5,\ldots}^{\infty}\frac{\tanh(i\pi\alpha/2)}{i^5\alpha}\right] \tag{10.a}$$

$$c_F=0 \tag{10.b}$$

where ε is the porosity of the porous channel, b is the width of the channel formed by two adjacent plate fins (see Fig. 1), and $\alpha=d/b$ is the aspect ratio of the channel formed by two adjacent plate fins. The infinite sum of Eq. (10.a) was truncated at i = 21 (11 terms), which yields results with at least six fully converged digits.

The specific surface area is given by,

$$a_{fs}=\frac{2\alpha+1}{\alpha}\frac{\varepsilon}{b} \tag{11}$$

The thermal conductivities of the solid and fluid phases in both the x- and y-directions can be calculated as,

$$k_{se,x}=k_{se,y}=k_s(1-\varepsilon) \tag{12.a.b}$$

$$k_{fe,x}=k_{fe,y}=k_f\varepsilon \tag{12.c.d}$$

where k_s is the thermal conductivity of the solid and k_f is the thermal conductivity of the fluid. Eqs. (12.a-d) assume the solid and fluid phases are disposed parallel with each other in both x- and y-directions.

The interstitial Nusselt number for thermally developing laminar flow in the channels formed by the plate fins can be obtained as described in section S1.1 (see Supplementary Information). Then, the interstitial heat transfer coefficient is given by,

$$h_{fs}=Nu_{fs}\frac{k_f}{D_h} \tag{13}$$

where Nu_{fs} is the interstitial Nusselt number and D_h is the hydraulic diameter of the channels formed by the plate fins.

2.2.2. Pin fins

The permeability for the pin fins case is determined by adjusting the Carman-Kozeny relation to the results of Zukauskas [36] (see section S1.2 of Supplementary Information). This procedure was shown to correctly predict the trend of the results from Zukauskas [8], even though the value of the adjusted coefficient adopted here differs from the one reported in that work to better fit the data. The inertial coefficient, c_F, is also adjusted to the same data. The results are as follows:

$$K = \frac{\varepsilon^3}{221(1-\varepsilon)^2} {d_c}^2 \tag{14.a}$$

$$c_F = 0.100 \tag{14.b}$$

where d_c is the pin diameter (see Fig. 1).

The specific surface area for the pin fins heat sink, defined as the ratio between the total surface area of the pins and the volume of the porous medium channel, is then,

$$a_{fs} = \frac{4(1-\varepsilon)}{d_c} \tag{15}$$

The thermal conductivities in the y-direction are determined using relations appropriate for parallel phases. For the x-direction, a relation from the literature is used [37] together with the assumption that the thermal conductivity of the solid is much larger than that of the fluid, yielding,

$$k_{se,x} = 0; k_{se,y} = k_s(1-\varepsilon) \tag{16.a.b}$$

$$k_{fe,x} = k_f\left(1 + 2\frac{1-\varepsilon}{\varepsilon}\right); k_{fe,y} = k_f\varepsilon \tag{16.c.d}$$

The interstitial heat transfer coefficient is obtained using the correlations proposed by Zukauskas [36] for staggered rows of cylinders in the following way:

$$h_{fs} = \frac{k_f}{d_c} C {Re_{d_c}}^m Pr^{0.36} \tag{17.a}$$

with,

$$Re_{d_c} = \frac{\rho u_{\max} d_c}{\mu} = \frac{\sqrt{\pi}}{\sqrt{\pi} - 2(1-\varepsilon)^{1/2}} \frac{\rho u d_c}{\mu} \tag{17.b}$$

where Re_{d_c} is the Reynolds number based on the fin diameter, Pr is the Prandtl number of the fluid, and $u_{\max}$ is the maximum interstitial velocity. The values for the constants C and m vary depending on the range of Reynolds numbers [36].

2.2.3. Metal foams

The fiber diameter can be determined from the pore diameter of the metal foam structure in the following way [38]:

$$d_{fib} = d_p \frac{1.18}{G}\sqrt{\frac{1-\varepsilon}{3\pi}} \tag{18.a}$$

with,

$$G = 1 - \exp\left(-\frac{1-\varepsilon}{0.04}\right) \tag{18.b}$$

where d_{fib} is the fiber diameter (see Fig. 1), d_p is the pore diameter (see Fig. 1), and G is a dimensionless factor that accounts for the change in the cross-section of the fiber with varying porosity [38].

The permeability, K, and the inertial coefficient, c_F, for metal foams are given by [39],

$$K = 0.00073(1-\varepsilon)^{-0.224}\left(\frac{d_{fib}}{d_p}\right)^{-1.11} {d_p}^2 \tag{19.a}$$

$$c_F = 0.00212(1-\varepsilon)^{-0.132}\left(\frac{d_{fib}}{d_p}\right)^{-1.63} \tag{19.b}$$

The specific surface area for metal foams is then [38],

$$a_{fs} = \frac{3\pi d_{fib} G}{(0.59 d_p)^2} \tag{20}$$

The thermal conductivities for metal foams are considered isotropic and can be, already including thermal dispersion effects, calculated as [40],

$$k_{se,x} = k_{se,y} = k_s\left\{\frac{2}{\sqrt{3}}\left[\frac{3r\xi}{1+\xi} + \frac{3}{2}(1-r) + \frac{3\sqrt{3}}{4r\xi}\left(\frac{\sqrt{3}}{2} - \xi\right)\right]\right\}^{-1} \tag{21.a}$$

$$k_{fe,x} = k_{fe,y} = k_f\left\{\frac{2}{\sqrt{3}}\left[\frac{3r\xi}{2-\xi} + \frac{3\xi(1-r)}{3-2\xi} + \frac{3\sqrt{3}}{3\sqrt{3}-4r\xi}\left(\frac{\sqrt{3}}{2} - \xi\right)\right]\right\}^{-1} + k_d \tag{21.b}$$

with,

$$\xi = \frac{-r + \sqrt{r^2 + \frac{2\sqrt{3}}{3}(1-\varepsilon)\left[2 - r\left(1 + \frac{4}{\sqrt{3}}\right)\right]}}{\frac{2}{3}\left[2 - r\left(1 + \frac{4}{\sqrt{3}}\right)\right]} \tag{21.c}$$

$$k_d = 0.06\rho c_p u K^{1/2} \tag{21.d}$$

where k_d is the apparent thermal conductivity due to thermal dispersion. Originally, a value of $r = 0.09$ was proposed [40]. However, a survey with a larger amount of empirical results found that $r = 0.098$ better fits the data [41].

The interstitial heat transfer coefficient is then obtained with the following correlation [40],

$$h_{fs} = 0.52\frac{k_f}{d_{fib}}\left(\frac{\rho u d_{fib}}{\varepsilon\mu}\right)^{0.5}\left(\frac{\mu c_p}{k_f}\right)^{0.37} \tag{22}$$

2.3. Solution Methodology

The Generalized Integral Transform Technique (GITT) is employed in the solution of the heat transfer model of Eqs. (5.a-c) and Eqs. (6.a-h) [24,28]. A complete description of both the method and the computational procedure are provided as Supplementary Information (see section S2). Here, for further reference in the results and discussion section, the truncated inverse formulae used in the reconstruction of the fluid and solid temperatures are reproduced, as follows:

$$T_f(x,y) = \theta_f(x,y) + \sum_{i=1}^{N} \bar{T}_i(x)\tilde{\psi}_{f,i}(y) \tag{23.a}$$

$$T_s(x,y) = \theta_s(x,y) + \sum_{i=1}^{N} \bar{T}_i(x)\tilde{\psi}_{s,i}(y) \tag{23.b}$$

where θ_f and θ_s are the fluid and solid temperatures, respectively, under thermally developed flow conditions, N is the truncation order, $\tilde{\psi}_{f,i}$ and $\tilde{\psi}_{s,i}$ are the normalized eigenfunctions for the fluid and solid temperature fields, respectively, and $\bar{T}_i$ is the transformed temperature field. The fully developed flow solutions are employed as analytical filters that satisfy and homogenize the boundary conditions of the original problem, while the eigenfunction expansions at the rightmost hand side of Eqs. (23.a,b) account for the thermally developing region contributions. The eigenfunctions are obtained from the following coupled eigenvalue problem, adapted from [28],

$$k_{se,y}\frac{d^2\psi_{s,i}}{dy^2} - a_{fs}h_{fs}\left(\psi_{s,i} - \psi_{f,i}\right) = 0 \tag{24.a}$$

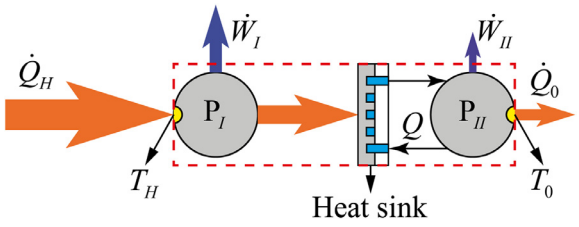

Fig. 2. Thermodynamic analysis of a two processes system featuring an intermediary heat sink. Red dashed enclosing representing the boundary of the system. Heat and power interactions are also indicated. (For interpretation of the references to color in this figure legend, the reader is referred to the web version of this article)

$$k_{fe,y}\frac{d^2\psi_{f,i}}{dy^2}+\omega_i{}^2\rho c_p u\psi_{f,i}(y)-a_{fs}h_{fs}\left(\psi_{f,i}-\psi_{s,i}\right)=0 \tag{24.b}$$

with boundary conditions and normalization given by,

$$\psi_{s,i}(0)=\psi_{f,i}(0);k_{fe,y}\left.\frac{d\psi_{f,i}}{dy}\right|_{y=0}+k_{se,y}\left.\frac{d\psi_{s,i}}{dy}\right|_{y=0}=0 \tag{24.c.d}$$

$$\left.\frac{d\psi_{f,i}}{dy}\right|_{y=d}=\left.\frac{d\psi_{s,i}}{dy}\right|_{y=d}=0 \tag{24.e.f}$$

$$\tilde{\psi}_{f,i}(y)=\frac{\psi_{f,i}(y)}{\sqrt{N_i}};\tilde{\psi}_{s,i}(y)=\frac{\psi_{s,i}(y)}{\sqrt{N_i}} \tag{24.g.h}$$

$$N_i=\int_0^d \rho c_p u\psi_{f,i}(y)^2dy \tag{24.i}$$

which leads to the orthogonality property below, that is essential in obtaining the transformed ordinary differential system for the transformed potentials,

$$\int_0^d \rho c_p u\tilde{\psi}_{f,i}(y)\tilde{\psi}_{f,j}(y)dy=\delta_{ij} \tag{25}$$

where δ_{ij} is Kronecker's delta.

The thermophysical properties necessary to solve the fluid flow and heat transfer models are interpolated from tables for pure water available in the literature [42]. The temperature used in the interpolation is the arithmetic mean between the mean fluid temperatures at the inlet ($T_m(0)$) and at the outlet ($T_m(L)$). The solid phase is considered to be Aluminum 6201 ($k_s = 205$W/mK [41]). The solution methodology was programmed in the Wolfram Mathematica v.12 [43] environment to ease the algebraic manipulations and to perform the numerical computations.

2.4. Optimization procedure

2.4.1. Entropy Generation Minimization

The purpose of this section is to briefly comment key aspects from the EGM method [7] and also to support its use instead of alternative design procedures. A two-process system is envisioned in this work, as illustrated in Fig. 2. A primary process, identified in Fig. 2 as P_I, is responsible for converting the heat transfer rate $\dot{Q}_H$ from a primary source, which can be fuel, sunlight, among others, into useful power $\dot{W}_I$; inevitably, heat is rejected as a by-product. This waste heat, usually severely depleted of free energy and named low-grade for this reason, is to be harnessed in a secondary process that will deliver more power $\dot{W}_{II}$ and finally reject heat to a reservoir with temperature T_0. The heat sink acts as an intermediary thermal device receiving the waste heat from the primary process and delivering it to the secondary process through the flow of a coolant, where Q is the volumetric flow rate.

For the system delimited by the red dashed rectangle shown in Fig. 2, the First and Second Laws of Thermodynamics in steady state can be written as,

$$\dot{Q}_H-\dot{Q}_0-\dot{W}_I-\dot{W}_{II}=0 \tag{26.a}$$

$$\frac{\dot{Q}_H}{T_H}-\frac{\dot{Q}_0}{T_0}+\dot{S}_{ger}=0 \tag{26.b}$$

where $\dot{S}_{ger}$ is the entropy generation rate in the system.

Considering the primary heat source as fixed, it is possible to eliminate $\dot{Q}_0$ by combining eqs. (26.a,b), yielding,

$$\dot{W}_I+\dot{W}_{II}=\left(1-\frac{T_0}{T_H}\right)\dot{Q}_H-T_0\dot{S}_{ger} \tag{27}$$

The rightmost term of Eq. (27) is strictly positive, which implies that, for a fixed primary heat source, it can be interpreted as a lost available work $\dot{W}_{lost}=T_0\dot{S}_{ger}\geq 0$; this result is widely known as Gouy-Stodola theorem [7]. Therefore, to ensure that the maximum power is delivered by the two processes, one must minimize the entropy generation rate within the whole system. One strategy to accomplish this goal is to minimize the entropy generation rate associated with each component of the system [7], such as the heat sink. Of course, minimizing the entropy generation just for the heat sink is not sufficient, and the irreversibility of the primary and secondary processes ought to be minimized as well to achieve maximum combined power output. Nevertheless, to further substantiate the focus of this work in low-grade waste heat harvesting heat sinks, they were shown to play a large role in the efficient operation of water desalination using membrane distillation [5].

2.4.2. Objective function and constraints

Local entropy generation rate is related to temperatures and their associated gradients, and the viscous dissipation term as follows [36]:

$$\dot{S}'''_{ger}=\dot{S}'''_{ger,T}+\dot{S}'''_{ger,u} \tag{28.a}$$

with,

$$\dot{S}'''_{ger,T}=\frac{k_{fe,x}}{T_f{}^2}\left(\frac{\partial T_f}{\partial x}\right)^2+\frac{k_{se,x}}{T_s{}^2}\left(\frac{\partial T_s}{\partial x}\right)^2+\frac{k_{fe,y}}{T_f{}^2}\left(\frac{\partial T_f}{\partial y}\right)^2+\frac{k_{se,y}}{T_s{}^2}\left(\frac{\partial T_s}{\partial y}\right)^2+\frac{a_{fs}h_{fs}}{T_sT_f}\left(T_s-T_f\right)^2 \tag{28.b}$$

$$\dot{S}'''_{ger,u}=\frac{\Phi}{T_f} \tag{28.c}$$

where $\dot{S}'''_{ger}$ is the local entropy generation rate, $\dot{S}'''_{ger,u}$ is the local entropy generation rate associated with fluid flow, and $\dot{S}'''_{ger,T}$ is the local entropy generation rate associated with heat transfer. The last term on the right hand side of Eq. (28.b) is added to the original relation [36] to account for the interstitial heat transfer between the fluid and solid phases of the adopted LTNE formulation.

The average entropy generation rate per unit of planform area for the whole heat sink is then obtained as,

$$\dot{S}''_{ger,av}=\frac{1}{L}\int_0^d\int_0^L \dot{S}'''_{ger}dxdy \tag{29}$$

where $\dot{S}''_{ger,av}$ is the average entropy generation rate per unit of planform area.

The integral transform solutions expressed by Eqs. (23.a,b) can be directly substituted in the local entropy generation rate expressions, Eqs. (28.a-c), and then be numerically integrated to obtain the average entropy generation rate, Eq. (29). However,

more complicated and computationally intensive optimization algorithms than the one employed here would be required. In this context, even though results from the numerical integration will also be reported for verification purposes, an approximate average entropy generation rate shall be employed as the objective function for the optimization process. First, the temperatures in the denominator of each term of Eqs. (28.b,c) are in the absolute temperature scale; then, the magnitude of the variation these temperatures are expected to suffer along the heat sink will likely be much smaller than their absolute numerical values. This approximation is especially reasonable for low-grade waste heat sources and the associated small temperature differences. Therefore, a characteristic temperature, equal to $T_c = T_m(L/2)$, will be used in the denominator of each term of Eqs. (28.b,c). Moreover, simple closed form expressions for the average entropy generation rate are attainable if lower truncation orders are set in Eqs. (23.a,b) to approximate the temperature fields. The simplest possible proposal is the retention of only the thermally developed solution from Eqs. (23.a,b) in Eqs. (28.b,c), more specifically, setting $T_f \cong \theta_f$ and $T_s \cong \theta_s$. Further in the text, this approximation will be shown to be accurate enough near the optimum. We then have,

$$\dot{S}'''_{ger,T} \cong \frac{k_{fe,x}}{T_c^2}\left(\frac{\partial \theta_f}{\partial x}\right)^2 + \frac{k_{se,x}}{T_c^2}\left(\frac{\partial \theta_s}{\partial x}\right)^2 + \frac{k_{fe,y}}{T_c^2}\left(\frac{\partial \theta_f}{\partial y}\right)^2 + \frac{k_{se,y}}{T_c^2}\left(\frac{\partial \theta_s}{\partial y}\right)^2 + \frac{a_{fs}h_{fs}}{T_c^2}\left(\theta_s - \theta_f\right)^2 \tag{30.a}$$

$$\dot{S}'''_{ger,u} \cong \frac{\Phi}{T_c} \tag{30.b}$$

where T_c is the characteristic temperature evaluated as $T_m(L/2)$. An analytical expression resulting from the integration of Eq. (29) using Eqs. (30.a,b) as integrands is offered in the Supplemetary Information (see section S3).

Constraints are necessary in order to obtain meaningful and feasible designs from the optimization process. The constraints vary with the different internal morphologies of the heat sink, and stem from manufacturing restrictions, like aspect ratios and minimum feature sizes, and limitations of the models employed. In general, the height of the flow paths' cross-sections is imposed to be at most 10 times the width, and features should be at least 100 μm thick. More precise statements of the constraints adopted are presented in section S3 of the Supplementary Information. These values are reasonably representative of available microfabrication techniques [44] and may be adjusted to the manufacturing capabilities of a particular design group. The exception is metal foams, for which these restrictions together with model limitations would preclude any feasible design to be obtained. For this case, the restrictions were partially relaxed as can be seen in section S3 of Supplementary Information.

A fixed volume, relevant for a particular application, is established to be occupied by any of the internal structures illustrated in Fig. 1. This volume will then be substituted by an equivalent porous medium, enabling the use of the model and solution methodology previously described. In addition, the heat load, inlet temperature, and flow rates are fixed in the optimization process and treated as duty parameters imposed by either the primary or secondary processes depicted in Fig. 2. The optimization problem to be solved can then be stated as,

$$\text{Minimize } \dot{S}''_{ger,av} \tag{31.a}$$

subject to constraints,

$$l_m(\boldsymbol{\chi}) \leq 0, m = 1, 2, 3, ..., M \tag{31.b}$$

where $\boldsymbol{\chi}$ is the vector of design parameters, l_m is a function of the designed parameters used to establish the m-th constraint, and M is the total number of constraints.

2.4.3. Lagrangian and KKT conditions

A Lagrangian capable of conveying information on the objective function and the constraints described earlier can be written as,

$$\mathcal{L}(\boldsymbol{\chi}, \lambda_m) = \dot{S}''_{ger,av}(\boldsymbol{\chi}) + \sum_{m=1}^{M} \lambda_m l_m(\boldsymbol{\chi}) \tag{32}$$

where $\mathcal{L}$ is the Lagrangian and λ_m is the m-th Lagrange multiplier.

A set of equations to be used to find possible candidates for the constrained minimum of $\dot{S}''_{ger,av}$ can then be analytically obtained from Eq. (32), as follows,

$$\nabla_{\boldsymbol{\chi}} \mathcal{L}(\boldsymbol{\chi}, \lambda_m) = 0 \tag{33.a}$$

$$\frac{\partial \mathcal{L}}{\partial \lambda_m} = 0 \tag{33.b}$$

where $\nabla_{\boldsymbol{\chi}}$ is the gradient with respect to the design parameters.

To deal with the Lagrange multiplier method under inequalities constraints, at first, the unconstrained case is analyzed, i.e., all Lagrange multipliers λ_m are set to zero in Eq. (32) and then Eq. (33.a) is solved for the design parameters $\boldsymbol{\chi}$. Afterwards, all possible constrained cases are analyzed, in the limits of the inequalities. For this purpose, Eq. (33.a) is solved together with Eq. (33.b) and $l_m(\boldsymbol{\chi}) = 0$ written for each constraint to be imposed in the particular run, yielding the design parameters and the Lagrange multipliers associated with the imposed constraints. The remaining Lagrange multipliers associated with constraints not involved in the run are set to zero. The equations are solved numerically using the function FindRoot from the platform Wolfram Mathematica v.12 [43].

Each candidate obtained through the process described in the last paragraph is then checked using the Karush-Kuhn-Tucker (KKT) conditions [45]. Then, the positive semi-definiteness of the Hessian matrix evaluated at each candidate point is checked to ensure optimality. Among the candidates that fulfill all criteria, the one that presents the minimum value of $\dot{S}''_{ger,av}$ is returned as the solution of the optimization procedure. The KKT conditions are described in detail in section S4 of the Supplementary Information.

3. Results and discussion

3.1. Convergence and validation

Table 1 illustrates the GITT solution convergence of the Nusselt number at three selected positions along the heat sink and of the average entropy generation per unit of planform area with varying truncation order N. Only results for plate fins and pin fins are contemplated for the sake of brevity. For better visualization of the convergence behavior, a graph conveying information on the convergence of the Nusselt number and of the average entropy generation rate from Table 1 is provided as Fig. S5.a,b (see Supplementary Information). An optimized configuration for the physical situation of the core of the heat sink occupying a volume of 10 cm x 10 cm x 2 mm, being subject to a flow rate of 5 L/min, inlet temperature of 25°C, and a heat flux of 100 W/cm² is chosen to illustrate the convergence behavior. These parameters are representative of the application of the heat sink in the waste heat recovery of membrane distillation systems [46]. As can be seen, convergence of the entropy generation rate is satisfactory, with a four significant digits convergence being achieved with N = 120. On the other hand, the convergence of the Nusselt number is considerably slower, especially for longitudinal positions closer to the entrance. Nevertheless, for the worst case (plate fins and x = 1 mm), the local Nusselt number changes by only 0.5% when the truncation order is raised from 110 to 120, which was deemed satisfactory. In sum, N = 120 was employed in all further calculations performed in this work.

Table 1
Convergence of the Nusselt number and average entropy generation per unit of planform area for plate fins and pin fins. Results shown for the optimized configuration given a volume of 10 cm x 10 cm x 2 mm, flow rate of 5 L/min, and prescribed heat flux of 100 W/cm². Values of design parameters: for plate fins b = 200 μm and $\varepsilon = 0.514$; for pin fins $d_c = 909$ μm and $\varepsilon = 0.475$.

N	Nu						$\dot{S}''_{ger,av}$ (W/m²K)	
	$x = 1$mm		$x = 5$mm		$x = 10$mm			
	Plate fins	Pin fins	Plate fins	Pin fins	Plate fins	Pin fins	Plate fins	Pin fins
1	474.7	732.5	471.1	717.1	467.3	702.4	133.0	99.94
4	482.6	746.4	477.7	727.2	472.5	709.2	132.2	99.51
7	488.1	752.2	482.0	731.1	475.7	711.6	131.8	99.38
10	493.6	757.6	485.9	734.5	478.2	713.5	131.5	99.27
70	576.1	819.5	502.2	746.9	483.7	717.3	130.3	98.80
80	581.8	821.3	502.3	746.9	483.7	717.3	130.3	98.78
90	586.4	822.2	502.3	746.9	483.7	717.3	130.2	98.77
100	590.1	822.6	502.4	746.9	483.7	717.3	130.2	98.76
110	593.4	822.8	502.4	746.9	483.7	717.3	130.2	98.75
120	596.2	822.8	502.5	746.9	483.7	717.3	130.2	98.75

The model and the computational code developed were validated against experimental data for plate-fins- [34,47], pin-fins- [48], and metal-foams-based [40] heat sinks reported in the literature. Comparisons of the fluid flow and heat transfer results obtained in this work and the experimental data are offered in section S5 of the Supplementary Information. The agreement of the model, method and computational results with the ones stemming from three independent experimental results is overall fairly good, building confidence on the designed porous media and integral transform approaches here adopted.

3.2. Thermodynamic optimization

Two particular applications are chosen to illustrate the procedure. The first one, to be henceforth referred to as 'small heat sink' case, stems from the cooling of HCPV panels [3]. The volume occupied by the equivalent porous media as depicted in Fig. 1 is, for this case, 1 cm x 1 cm x 1 mm and the coolant flow rate is 35 mL/min. The second, coined as 'large heat sink' case, was already introduced in section 3.1, and is related to waste heat recovery for water desalination using membrane distillation [46]. In this case, the volume occupied by the porous medium channel is 10 cm x 10 cm x 2 mm and the flow rate is 5 L/min. For both cases, the inlet temperature is set to 25°C. The input parameters are summarized in section S6 (see Supplementary Information).

Fig. 3 offers the minimum average entropy generation rate per unit area, as a function of heat load, obtained through the optimization procedure described earlier. Both the approximate entropy generation rate, calculated with the thermally developed solution, and the complete entropy generation rate obtained through numerical integration of Eq. (29) together with Eqs. (23.a,b) and Eqs. (28.a-c) are depicted. A different optimized set of design parameters is obtained for each heat load considered. Figs. 3a and 3.b refer to the small and large heat sinks, respectively. As already mentioned, the restrictions stemming from manufacturing and model limitations hinder the optimization of the metal-foams-based heat sink. Thus, even though Figs. 3.a,b show a significant disadvantage of this morphology in comparison with both the plate and pin fins, the results from the optimization of the metal foams are ultimately considered to be inconclusive.

From the results of Figs. 3, it is possible to assert that the approximation introduced into the objective function is justified, since, near the optimum, the agreement between the complete and approximate formulations of the entropy generation is mostly good. The exceptions are heat sinks based on metal foams, for which the constraints became too restrictive to produce designs with performance comparable to plate and pin fins. In this case, the approximate entropy generation rate yields values up to 2x the one calculated with the fully converged temperature fields. For plate and pin fins, the deviation between approximate and complete entropy generation rate of the optimum internal arrangement stayed below 5% and 10% for the small and large heat sinks applications, respectively, thus corroborating the simplified optimization procedure proposed. In case more precise approximations are needed, additional terms from the eigenfunction expansions of Eqs. (23.a,b) can be added to the calculation of the entropy generation rate, which is an advantage of using a hybrid numerical-analytical scheme such as the GITT. For instance, Table 1 shows that the entropy generation rate obtained with the addition of just one more term to the fully developed temperature field (N = 1) deviate from the fully converged value by only 2% and 1% for the plate and pin fins, respectively.

For the small heat sink case, as can be seen in Fig. 3.a, the average entropy generation rates per unit of area obtained with plate and pin fins are roughly equivalent, especially given possible uncertainties in the models employed. For instance, when a heat flux of 100 W/cm² is applied, the entropy generation of the pin-fins-based heat sink is only 7% higher than the one associated with plate fins. The ease of manufacturing then dictates, in this case, that the plate fins should be selected. On the other hand, for the large heat sink case, according to Fig. 3.b, whether plate fins or pin fins should be used is dependent on the applied heat load. For lower heat loads, the plate fins have some advantage, while for higher heat loads, pin fins should be used. The data available in Table 1 further illustrates the advantage of pin fins for the large heat sinks subject to 100 W/cm², with a 24% lower entropy generation rate per unit area in comparison with the plate fins. The main reason for this behavior is the superior heat transfer capabilities of the pin fins design, at the expense of higher pressure drops; for lower heat loads, heat transfer loses importance and the plate fins become more advantageous.

Figs. 4a,b and Figs. 5a,b illustrate the behavior of the entropy generation rate with changes on the design parameters (porosity and channel width or pin diameter) and also the optimum points for the large heat sink case. When lower heat fluxes are applied, such as 1 W/cm² associated with Figs. 4.a,b, both the plate and pin fins optimum arrangements tend to higher porosities, which is an indicative of the dominance of the irreversibility associated with viscous dissipation that can be significantly reduced by providing more space for the fluid to flow. A minimum entropy generation rate point is found inside the region formed by the constraints, even though, for the plate fins, this optimum point is relatively close to the curve representing the minimum fin thickness allowed

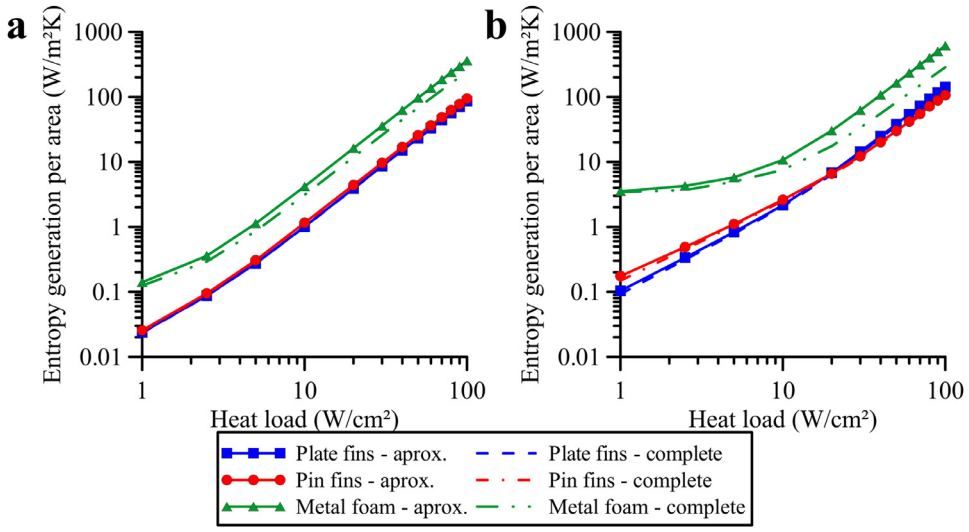

Fig. 3. Entropy generation rate per unit of planform area as a function of heat load. (a) Small heat sink; (b) Large heat sink. 'Approximate' curves refer to values obtained with Eqs. (30.a,b), while 'complete' curves refer to values obtained numerically with Eqs. (28.a-c) and Eq. (29).

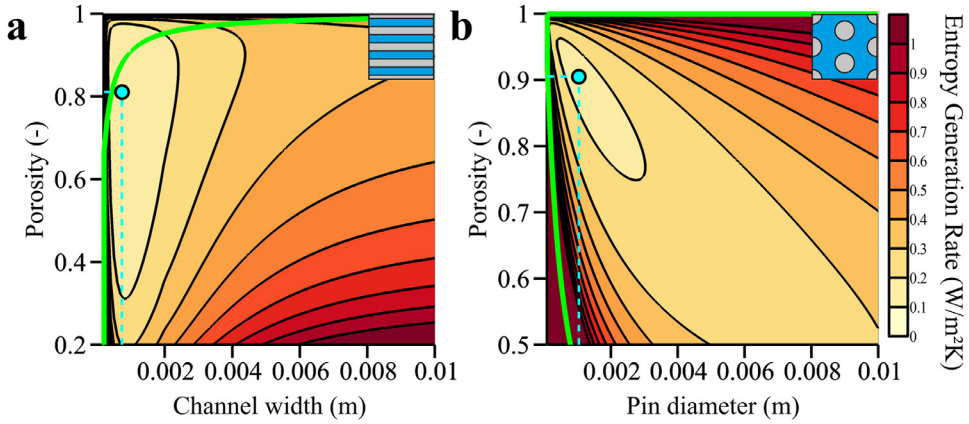

Fig. 4. Contours of entropy generation rate per unit of planform area for a heat load of 1 W/cm². (a) Plate fins; (b) Pin fins. Point and dashed lines indicating the optimum point location. Thick green solid lines indicating the constraints. The insets represent the geometries associated with each graph. (For interpretation of the references to color in this figure legend, the reader is referred to the web version of this article)

by manufacturing restrictions (100 μm). For a heat load equal to 100 W/cm², Figs. 5.a,b show that the optimum design parameters points lie on curves representing constraints; more specifically, plate and pin fins become limited by a maximum aspect ratio of the flow path, as detailed in sections 2.4.2 and S3 (see Supplementary Information). Furthermore, the optimum design parameters for 100 W/cm² tend to lower porosities, for the associated narrower flow paths improve the heat transfer performance, which is the limiting factor under high heat loads.

The optimum sizing parameters that are either design parameters themselves or quantities derived from the design parameters are shown in Figs. 6.a,b for the large heat sink case. As the heat load decreases, both the channel width b and the pin spacing s (see Fig. 1) significantly increase, broadening the cross-section of the flow path, thereby reducing fluid-friction-related irreversibility. The thickness of the plate fin initially decreases with increasing heat load. However, at some point, the tendency reverses, and a higher value is attained, as shown in Fig. 6.a. On the other hand, the optimum pin fin diameter shows a reverse behavior, initially rising slightly and then decreasing mildly. A similar pattern to the one observed for the pin diameter is present for both the number of channels and number of pins; the difference is that the initial rise is considerably steeper than the one seen in the pin diameter case.

3.3. Shortcomings of a common design procedure

Fig. 7a presents a graph commonly used in heat sink design [49]. In this graph, the flow rate is varied and the resulting thermal resistance and pumping power are plotted for both the plate and pin fins large heat sinks with a heat flux of 100 W/cm² imposed at the bottom wall. From these curves alone, a designer may decide to select the plate fins as the more appropriate internal morphology for low-grade waste heat harvesting, since, for a given pumping power, the thermal resistance is lower using plate fins instead of pin fins. Nevertheless, the results of Fig. 3.b and Table 1 point to a significant advantage of the pin fins over the plate fins in this particular case.

To understand these conflicting conclusions, a metric named Bejan number is employed. This dimensionless number is simply the ratio of the local entropy generation rate due to heat transfer and the total local entropy generation rate [50]. Mathematically,

$$Be = \frac{\dot{S}'''_{ger,T}}{\dot{S}'''_{ger,T} + \dot{S}'''_{ger,u}} \tag{34}$$

where Be is the Bejan number.

Contours of the Bejan number for the large heat sink case with an applied heat flux of 1 W/cm² are illustrated in Fig. 8.a,b for plate and pin fins, respectively. Given the relatively low heat load,

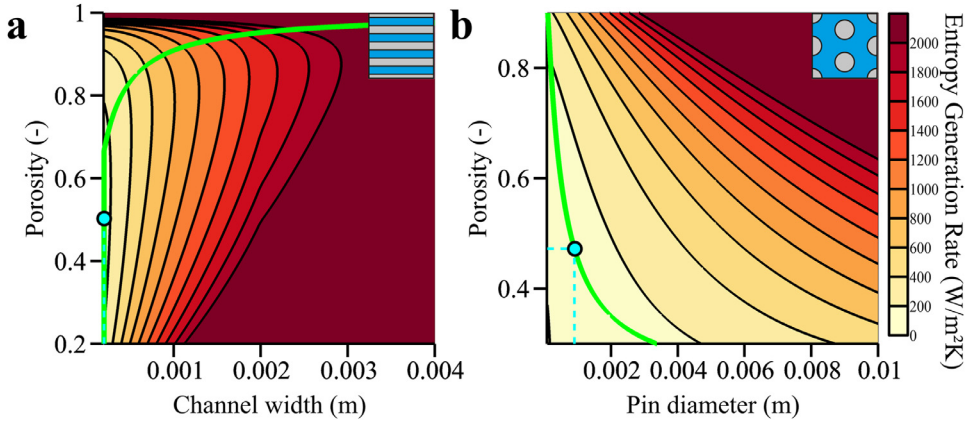

Fig. 5. Contours of entropy generation rate per unit of planform area for a heat load of 100 W/cm². (a) Plate fins; (b) Pin fins. Point and dashed lines indicating the optimum point location. Thick green solid lines indicating the constraints. The insets represent the geometries associated with each graph. (For interpretation of the references to color in this figure legend, the reader is referred to the web version of this article)

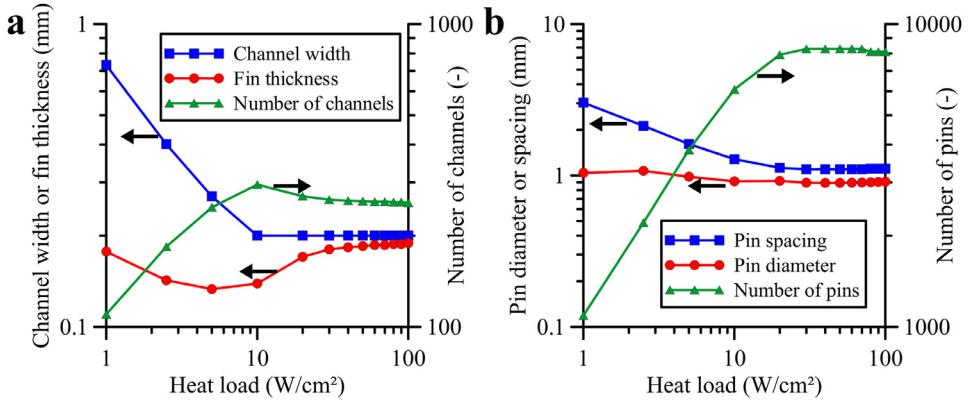

Fig. 6. Optimum sizing of the plate and pin fins for the large heat sink application. (a) Plate fins; (b) Pin fins.

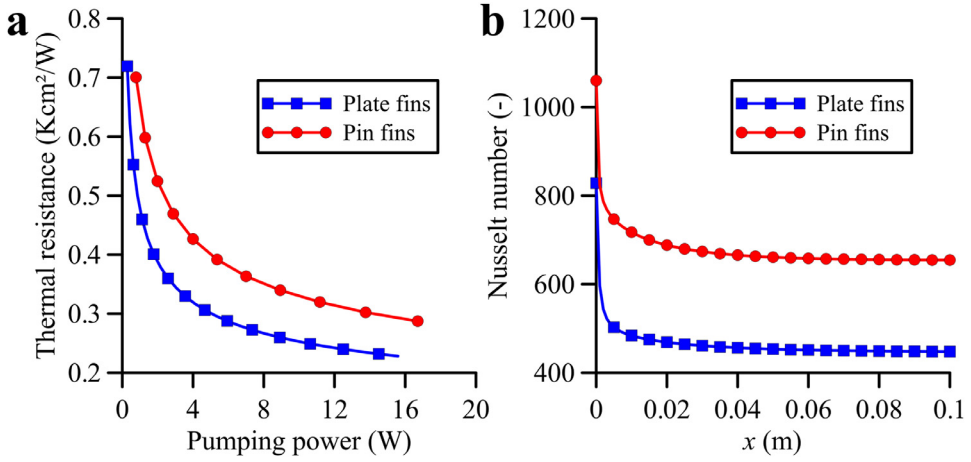

Fig. 7. Thermal resistance, pumping power, and Nusselt number for the optimum designs of plate and pin fins large heat sinks subject to a heat load of 100 W/cm². (a) Thermal resistance versus pumping power for varying flow rate; (b) Local Nusselt number as a function of longitudinal position (x) for a fixed flow rate (5 L/min).

the irreversibility is more evenly split between viscous dissipation and heat transfer, favoring designs with lower associated pumping power; in this case, the plate fins. Fig. 9 shows Bejan number contours for the pin fins heat sink subject to a heat load of 100 W/cm²; plate fins are not contemplated, for, in the same scale of the graph for pin fins, it renders a blank figure due to all values being above 0.99. In this situation, the relatively large heat load causes a complete dominance of the heat-transfer-related irreversibility. Thus, in this case, heat transfer performance should be emphasized over pumping power, given the centrality of minimizing the entropy generation rate established in section 2.4.1. Fig. 7b shows a significant advantage of the pin fins design as far as heat transfer is concerned, and that is the reason for preferring the pin fins as indicated by Fig. 3.b.

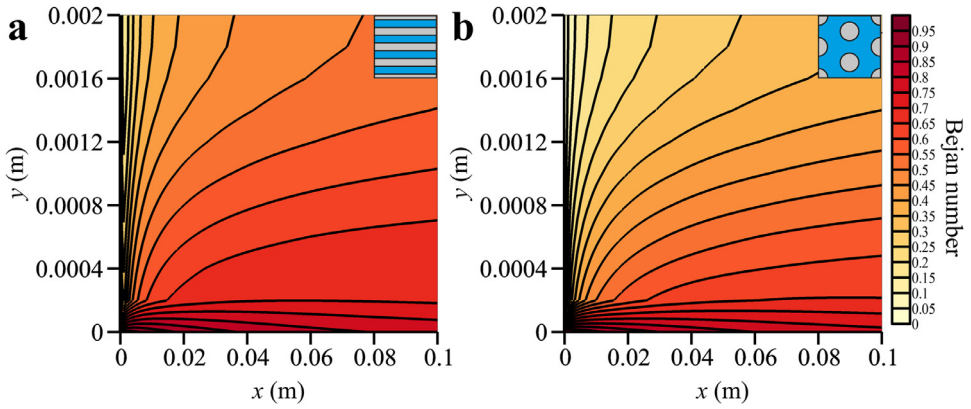

Fig. 8. Contours of the Bejan number for the large heat sink case subject to a heat load of 1 W/cm². (a) Plate fins; (b) Pin fins. The insets represent the geometries associated with each graph.

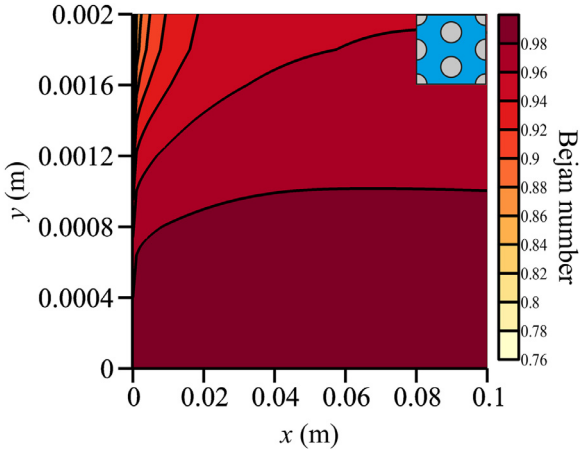

Fig. 9. Contours of the Bejan number for the large heat sink case with pin fins subject to a heat load of 100 W/cm². The inset represents the geometry associated with the graph.

4. CONCLUSIONS

A comprehensive heat sinks design procedure intended for low-grade waste heat harvesting was proposed, implemented, and illustrated. The combination of the designed porous medium concept and the EGM method allowed for the treatment of different internal morphologies of the heat sink within a unified framework.

For the application involving small heat sinks, stemming from cooling of HCPV panels, the use of plate and pin fins were shown to be roughly equivalent as far as destroying the least amount of available work is concerned. For the application with large heat sinks, associated with heat recovery for membrane distillation, the best design is strongly dependent on the heat load imposed on the heat sink. Large heat loads favored the use of pin fins, while plate fins are preferred for low heat loads. This conclusion enters into conflict with a comparison based on thermal resistance versus pumping power curves, which predicts that plate fins are a superior design. For instance, a plate-fins-based heat sink has a thermal resistance of 0.276 Kcm²/W as opposed to 0.363 Kcm²/W obtained with pin fins for a pumping power of 7 W. However, an optimized plate fins heat sink destroys roughly 24% more exergy than one employing pin fins when a heat flux of 100 W/cm² is imposed. This problem is then clarified by showing that, at such high heat loads, heat transfer should be emphasized at the expense of pumping power. Therefore, unless the pumping power is a given duty parameter for a particular application, the EGM method is a more reliable source of optimum designs for heat sinks intended for low-grade waste heat recovery. The entropy generation rate is capable of automatically conveying information on heat transfer and fluid flow and selecting which one should take precedence without the introduction of artificial figures of merit for this purpose.

The optimization analysis of the metal-foam-based heat sink was inconclusive, for the constraints related to manufacturing and models hinder the attainment of similar performance figures as obtained with the plate and pin fins. Since the modeling restrictions may stem from the limited data they are based on, rather than the design itself, no further critical analysis was pursued for this case.

In order to be fully effective, the entropy generation must also be minimized for the primary and secondary processes coupled with the heat sink, which shall be done in the near future. A possible symbiotic relation between a hybrid numerical-analytical approach, such as the GITT, and the EGM method of thermodynamic optimization was identified in this work, and shall be pursued further in future endeavors.

Declaration of Competing Interest

The authors declare that they have no known competing financial interests or personal relationships that could have appeared to influence the work reported in this paper.

CRediT authorship contribution statement

Kleber Marques Lisboa: Conceptualization, Methodology, Software, Formal analysis, Writing – original draft, Writing – review & editing, Visualization, Funding acquisition. **José Luiz Zanon Zotin:** Methodology, Formal analysis, Visualization. **Carolina P. Naveira-Cotta:** Conceptualization, Writing – review & editing, Supervision, Project administration, Funding acquisition. **Renato Machado Cotta:** Conceptualization, Writing – review & editing, Supervision, Project administration, Funding acquisition.

ACKNOWLEDGEMENTS

The authors are grateful for the financial support offered by the Brazilian Government agencies CNPq, CAPES (PROCAD/DEFESA), and FAPERJ (Grant no. E-26/010/002590/2019).

Supplementary materials

Supplementary material associated with this article can be found, in the online version, at doi:10.1016/j.ijheatmasstransfer.2021.121850.

References

[1] H. Fang, J. Xia, Y. Jiang, Key issues and solutions in a district heating system using low-grade industrial waste heat, Energy 86 (2015) 589-602. https://doi.org/10.1016/j.energy.2015.04.052

[2] S. Zimmermann, M.K. Tiwari, G.I. Meijer, B. Michel, D. Poulikakos, Aquasar: a hot water cooled data center with direct energy reuse, Renew. Energy 43 (2012) 237–245, doi:10.1016/j.energy.2012.04.037.

[3] S. Zimmermann, H. Helmers, M.K. Tiwari, S. Paredes, B. Michel, M. Wiesenfarth, A.W. Bett, D. Poulikakos, A high-efficiency hybrid high concentration photovoltaic system, Int. J. Heat Mass Transf. 89 (2015) 514–521, doi:10.1016/j.ijheatmasstransfer.2015.04.068.

[4] S. Araya, A.P. Wemhoff, G.F. Jones, A.S. Fleischer, An experimental study of an Organic Rankine Cycle utilizing HCFO-1233zd(E) as a drop-in replacement for HFC-245fa for ultra-low-grade waste heat recovery, Appl. Thermal Eng. 180 (2020) 115757, doi:10.1016/j.applthermaleng.2020.115757.

[5] K.M. Lisboa, D.B. Moraes, C.P. Naveira-Cotta, R.M. Cotta, Analysis of the membrane effects on the energy efficiency of water desalination in a direct contact membrane distillation (DCMD) system with heat recovery, Appl. Thermal Eng. 182 (2021) 116063, doi:10.1016/j.applthermaleng.2020.116063.

[6] K. Imasato, S.D. Kang, G.J. Snyder, Exceptional thermoelectric performance in $Mg_3Sb_{0.6}Bi_{1.4}$ for low-grade waste heat recovery, Energy Environ. Sci. 12 (2019) 965–971, doi:10.1039/C8EE03374A.

[7] A. Bejan, Entropy Generation Minimization: The Method of Thermodynamic Optimization of Finite-Size Systems and Finite-Time Processes, 1st ed., CRC Press, Boca Raton, FL, 1996.

[8] A. Bejan, A. Morega, Optimal arrays of pin fins and plate fins in laminar forced convection, J. Heat Transfer 115 (1993) 75–81, doi:10.1115/1.2910672.

[9] W. Escher, B. Michel, D. Poulikakos, A novel high performance, ultra thin heat sink for electronics, Int. J. Heat Fluid Flow 31 (2010) 586–598, doi:10.1016/j.ijheatfluidflow.2010.03.001.

[10] F. Alfieri, M.K. Tiwari, I. Zinovik, D. Poulikakos, 3D integrated water cooling of a composite multilayer stack of chips, J. Heat Transfer 132 (2010) 121402, doi:10.1115/1.4002287.

[11] J.R. Culham, Y.S. Muzychka, Optimization of plate fin heat sinks using entropy generation minimization, IEEE Trans. Compon. Packaging Technol. 24 (2001) 159–165, doi:10.1109/6144.926378.

[12] W.A. Khan, J.R. Culham, M.M. Yovanovich, Optimization of microchannel heat sinks using entropy generation minimization methods, IEEE Trans. Compon. Packaging Technol. 32 (2009) 243–251, doi:10.1109/TCAPT.2009.2022586.

[13] W.A. Khan, J.R. Culham, M.M. Yovanovich, Optimization of pin-fin heat sinks using entropy generation minimization, IEEE Trans. Compon. Packaging Technol. 28 (2005) 247–254, doi:10.1109/TCAPT.2005.848507.

[14] L. Chen, A. Yang, Z. Xie, F. Sun, Constructal entropy generation rate minimization for cylindrical pin-fin heat sinks, Int. J. Thermal Sci. 111 (2017) 168–174, doi:10.1016/j.ijthermalsci.2016.08.017.

[15] K. Hooman, H. Gurgenci, A.A. Merrikh, Heat transfer and entropy generation optimization of forced convection in porous-saturated ducts of rectangular cross-section, Int. J. Heat Mass Transf. 50 (2007) 2051–2059, doi:10.1016/j.ijheatmasstransfer.2006.11.015.

[16] M. Odabaee, K. Hooman, Application of metal foams in air-cooled condensers for geothermal power plants: An optimization study, Int. Commun. Heat Mass Transf. 38 (2011) 838–843, doi:10.1016/j.icheatmasstransfer.2011.03.028.

[17] W.W. Wang, Y. Cai, L. Wang, C.-W. Liu, F.-Y. Zhao, D. Liu, Thermo-hydrodynamic analytical model, numerical solution and experimental validation of a radial heat pipe with internally finned condenser applied for building heat recovery units, Energy Convers. Manag. 219 (2020) 113041, doi:10.1016/j.enconman.2020.113041.

[18] A. Bejan, Designed porous media: Maximal heat transfer density at decreasing length scales, Int. J. Heat Mass Transf. 47 (2004) 3073–3083, doi:10.1016/j.ijheatmasstransfer.2004.02.025.

[19] S.Y. Kim, A.V. Kuznetsov, Optimization of pin-fin heat sinks using anisotropic local thermal nonequilibrium porous model in a jet impinging channel, Numer. Heat Transf. Part A – Appl 44 (2003) 771–787, doi:10.1080/716100528.

[20] L. Wang, W.-W. Wang, Y. Cai, D. Liu, F.-Y. Zhao, Effects of porous fins on mixed convection and heat transfer mechanics in lid-driven cavities: Full numerical modeling and parametric simulations, Transp. Porous Med. 132 (2020) 495–534, doi:10.1007/s11242-020-01402-3.

[21] Y. Mahmoudi, N. Karimi, K. Mazaheri, Analytical investigation of heat transfer enhancement in a channel partially filled with a porous material under local thermal non-equilibrium condition: Effects of different thermal boundary conditions at the porous-fluid interface, Int. J. Heat Mass Transf. 70 (2014) 875–891, doi:10.1016/j.ijheatmasstransfer.2013.11.048.

[22] A. Amiri, K. Vafai, Analysis of dispersion effects and non-thermal equilibrium, non-Darcian, variable porosity incompressible flow through porous media, Int. J. Heat Mass Transf. 37 (1994) 939–954, doi:10.1016/0017-9310(94)90219-4.

[23] Y. Mahmoudi, N. Karimi, Numerical investigation of heat transfer enhancement in a pipe partially filled with a porous material under local thermal non-equilibrium condition, Int. J. Heat Mass Transf. 68 (2014) 161–173, doi:10.1016/j.ijheatmasstransfer.2013.09.020.

[24] R.M. Cotta, Hybrid numerical-analytical approach to nonlinear diffusion problems, Numer. Heat Transfer – Part B Fund. 127 (1990) 217–226 http://doi.org/10.1080/10407799008961741.

[25] R.M. Cotta, Integral Transforms in Computational Heat and Fluid Flow, 1st ed., CRC Press, Boca Raton, FL, 1993.

[26] H.Luz Neto, J.N.N. Quaresma, R.M. Cotta, Natural convection in three-dimensional porous cavities: Integral transform method, Int. J. Heat Mass Transf. 45 (2002) 3013–3032, doi:10.1016/s0017-9310(02)00015-7.

[27] K.M. Lisboa, J. Su, R.M. Cotta, Single domain integral transforms analysis of natural convection in cavities partially filled with heat generating porous medium, Numer. Heat Transf. – Part A Appl 74 (2018) 1068–1086, doi:10.1080/10407782.2018.1511141.

[28] K.M. Lisboa, J.L.Z. Zotin, R.M. Cotta, Hybrid solutions for thermally developing flows in channels partially filled with porous media, Numer. Heat Transf. – Part B Fund 79 (2021) 189–215, doi:10.1080/10407790.2020.1819700.

[29] S. Whitaker, Flow in porous media I: A theoretical derivation of Darcy's law, Transp. Porous Med. 1 (1986) 3–25, doi:10.1007/BF01036523.

[30] J.-L. Auriault, On the domain of validity of Brinkman's equation, Transp. Porous Med. 79 (2009) 215–223, doi:10.1007/s11242-008-9308-7.

[31] D.A. Nield, Resolution of a paradox involving viscous dissipation and nonlinear drag in a porous medium, Transp. Porous Med. 41 (2000) 349–357, doi:10.1023/A:1006636605498.

[32] K. Vafai, K. Yang, A note on local thermal non-equilibrium in porous media and heat flux bifurcation phenomenon in porous media, Transp. Porous Med. 96 (2013) 169–172, doi:10.1007/s11242-012-0080-3.

[33] B. Alazmi, K. Vafai, Constant wall heat flux boundary conditions in porous media under local thermal non-equilibrium conditions, Int. J. Heat Mass Transf. 45 (2002) 3071–3087, doi:10.1016/S0017-9310(02)00044-3.

[34] P.-S. Lee, S.V. Garimella, D. Liu, Investigation of heat transfer in rectangular microchannels, Int. J. Heat Mass Transf. 48 (2005) 1688–1704, doi:10.1016/j.ijheatmasstransfer.2004.11.019.

[35] R.K. Shah, A.L. London, Laminar Flow Forced Convection in Ducts, Advances in Heat Transfer, Supplement 1, Academic Press, New York, NY, 1978.

[36] A. Bejan, Convection Heat Transfer, 4th ed., Wiley, New Jersey, NJ, 2013.

[37] J.W. Strutt, On the influence of obstacles arranged in rectangular order upon the properties of a medium, Philos. Mag. 5 (1892) 481–502, doi:10.1080/14786449208620364.

[38] A. Bhattacharya, V.V. Calmidi, R.L. Mahajan, Thermophysical properties of high porosity metal foams, Int. J. Heat Mass Transf. 45 (2002) 1017–1031, doi:10.1016/S0017-9310(01)00220-4.

[39] S. Mahjoob, K. Vafai, A synthesis of fluid and thermal transport models for metal foam heat exchangers, Int. J. Heat Mass Transf. 51 (2008) 3701–3711, doi:10.1016/j.ijheatmasstransfer.2007.12.012.

[40] V.V. Calmidi, R.L. Mahajan, Forced convection in high porosity metal foams, J. Heat Transfer 122 (2000) 557–565, doi:10.1115/1.1287793.

[41] P. Ranut, On the effective thermal conductivity of aluminum metal foams: Review and improvement of the available empirical and analytical models, Appl. Therm. Eng. 101 (2016) 496–524, doi:10.1016/j.applthermaleng.2015.09.094.

[42] D.R. Lide, W.M. Haynes, Handbook of Chemistry and Physics, 90th ed., CRC Press, Boca Raton, FL, 2010.

[43] S. Wolfram, Wolfram Mathematica 12 (2019).

[44] M.J. Madou, Fundamentals of Microfabrication: The Science of Miniaturization, 2nd ed., CRC Press, Boca Raton, FL, 2002.

[45] S. Boyd, L. Vandenberghe, Convex Optimization, 1st ed., Cambridge University Press, Cambridge, UK, 2004.

[46] O. Andrjesdóttir, C.L. Ong, M. Nabavi, S. Paredes, A.S.G. Khalil, B. Michel, D. Poulikakos, An experimentally optimized model for heat and mass transfer in direct contact membrane distillation, Int. J. Heat Mass Transf. 66 (2013) 855–867, doi:10.1016/j.ijheatmasstransfer.2013.07.051.

[47] D. Liu, S.V. Garimella, Investigation of liquid flow in microchannels, J. Thermophys. Heat Transf. 18 (2004) 65–72, doi:10.2514/1.9124.

[48] A. Kosar, Y. Peles, Thermal-hydraulic performance of MEMS-based pin fin heat sink, J. Heat Transfer 128 (2006) 121–131, doi:10.1115/1.2137760.

[49] K. Boomsma, D. Poulikakos, F. Zwick, Metal foams as compact high performance heat exchangers, Mech. Mater. 35 (2003) 1161–1176, doi:10.1016/j.mechmat.2003.02.001.

[50] E. Sciubba, A minimum entropy generation procedure for the discrete pseudo-optimization of finned-tube heat exchangers, Rev. Gén. Therm. 35 (1996) 517–525, doi:10.1016/S0035-3159(99)80079-8.